

Double Degree Nanoquad Master Thesis

# Modelling and experimental characterization of a quantum well photodetector at $9 \mu m$

Andrea Piazza

Paris, June 15, 2023



ENS internship Supervisor:

Prof. Angela Vasanelli

Polytechnic of Turin Academic supervisor:

Prof. Carlo Ricciardi

Université Paris cité Academic supervisor:

Prof. Maria Luisa Della Rocca



# Contents

<b>1</b>	<b>Introduction</b>	<b>4</b>
<b>2</b>	<b>Theoretical background</b>	<b>5</b>
2.1	Quantum wells . . . . .	5
2.2	Theoretical description of a QWIP . . . . .	8
2.2.1	3D Model . . . . .	10
2.2.2	Emission capture model . . . . .	10
2.2.3	Photocurrent . . . . .	11
2.2.4	Responsivity . . . . .	12
<b>3</b>	<b>Experimental Analysis</b>	<b>14</b>
3.1	Device details . . . . .	14
3.1.1	Absorption profile . . . . .	16
3.2	Mesa geometry . . . . .	20
3.3	I/V characteristic . . . . .	21
3.3.1	Dark current . . . . .	21
3.3.2	Photocurrent . . . . .	23
3.4	Spectral characterization of the QWIP. . . . .	25
3.4.1	Voltage dependence . . . . .	25
3.4.2	Temperature dependence . . . . .	27
3.5	Responsivity . . . . .	28
<b>4</b>	<b>Conclusions</b>	<b>29</b>

# Chapter 1

## Introduction

The internship has been hosted by the Quantum Physics and Devices (QUAD) team at ENS in Paris. The team is mainly focused on exploiting quantum phenomena and concepts to design new optoelectronic devices in the mid and far-infrared (3-300  $\mu\text{m}$ ). The group has a large expertise in the field of light matter interaction for the realization of infrared photonic and plasmonic devices. The thesis work is mainly focused on detection of light, through 1D confined quantum systems, semiconductors quantum wells. The device that I have characterized is a quantum well infrared photodetector, made of  $Ga_{0.47}In_{0.53}As/(Ga_{0.47}In_{0.53}As)_{0.5} - (Al_{0.48}In_{0.52}As)_{0.5}$  lattice matched to  $InP : Fe$  substrate, working in the mid-Infrared spectrum (9 $\mu\text{m}$ ). It was epitaxially grown by the group of Isabelle Sagnes at C2N and fabricated by Livia Del Balzo, a Phd student in the QUAD group. The outcome of the work are among the first performed in the QUAD group with a quaternary material employed as barrier for  $InGaAs$  quantum wells. As a consequence, this analysis could be used as reference for the next implementations of the devices.

This thesis is divided in 3 main parts :

- The second chapter is related to the basic physical knowledge needed to study and understand the device working principle.
- The third chapter is focused on the QWIP that I have characterized and on the experimental results obtained.
- The fourth chapter is devoted to conclusions and perspectives.

## Chapter 2

# Theoretical background

This chapter is devoted to the basic physics principles and operation of a quantum well infrared photodetector (QWIP). The first section is mainly devoted to a description of Quantum Wells (QW). The second section is related to the two simple physical models used to describe the device. Both models have been employed to analyze QWIP devices, with good accordance between experimental and theoretical results. The references used for this chapter are [1],[2] and [3].

### 2.1 Quantum wells

Semiconductor quantum wells are the fundamental building blocks of QWIP devices. They allow confining electrons in one direction giving rise to a 2D electron gas. QWs are manufactured through the stacking of different layers of semiconductors with different band gaps and same lattice constant. The semiconductor with lower band gap acts as a potential well. If the dimension of the layer is less than the de Broglie wavelength of electrons, confinement is obtained in the growth direction of the heterostructure, resulting in the quantization of the energy levels. A schematic of a single type one QW is depicted in figure 2.1.

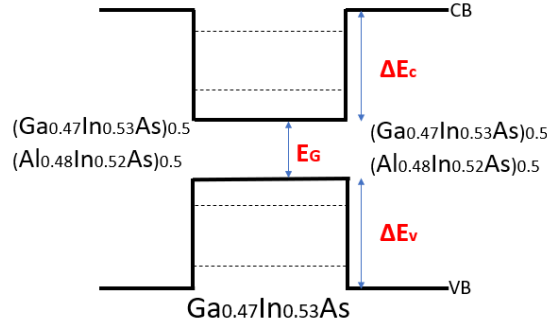


**Figure 2.1:** Schematic band diagram of a QW in the same material system used in this work.

The quantum mechanical problem is analyzed assuming a single electronic band (the conduction band) in a single particle approach. Within the envelope function approximation, the wavefunction can be written as:  $\psi_i(\vec{r}) = f_i(\vec{r})u_c(\vec{r})$ , where  $f_i(\vec{r})$  is the envelope function and  $u_c(\vec{r})$  is the Bloch function for the conduction band. The envelope function depends on the shape of the potential well and on external fields acting on the system and satisfies:

$$\frac{\hbar^2}{2m^*} \Delta f_i(\vec{r}) + V(\vec{r})f_i(\vec{r}) = E f_i(\vec{r}) \quad (2.1)$$

with  $m^*$  the effective mass and  $V(\vec{r})$  a slowly varying potential. Defining the direction of growth of the heterostructure, in this case  $z$ , it is possible to rewrite the envelope function as product of two contribution:

$$f_{n,k_\perp}(\vec{r}) = \frac{1}{\sqrt{A}} e^{i\vec{k}_\perp \cdot \vec{r}} \phi_n(z) \quad (2.2)$$

where  $\vec{k}_\perp$  is the in-plane wavevector,  $n$  is the index associated with the confined state in direction  $\vec{z}$  and  $A$  is the in-plane area. This allows solving the problem in  $\vec{x}-\vec{y}$  and  $\vec{z}$  independently, such that equation 2.1 reduces to a 1D form:

$$-\frac{\hbar^2}{2m^*} \frac{d^2}{dz^2} \phi_n(z) + V(z)\phi_n(z) = E_n \phi_n(z) \quad (2.3)$$

The eigenvalues of the system are found solving equation 2.3. For a constant effective mass and infinite barriers, the dispersion relation is found to be :

$$E_n = \frac{\hbar^2}{2m^*} \left( \frac{(\pi n)^2}{L_w^2} + k_\perp^2 \right) \quad (2.4)$$

where  $L_w$  is the well's thickness. The parameters needed to design the energy states, called subbands, are the well's length  $L_w$  and its height  $V_B$ . The dispersion relation could be split in plane and out of plane. A schematic of the electron dispersion is depicted in figure 2.2.

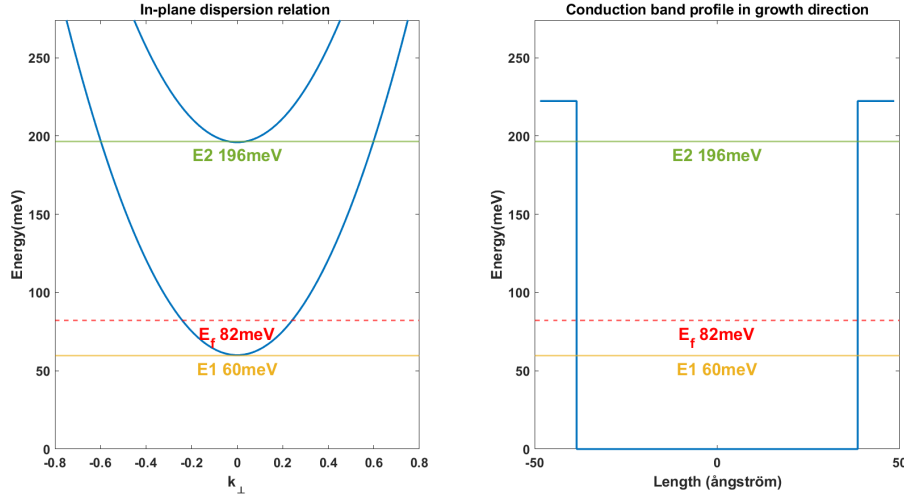


**Figure 2.2:** In-plane dispersion relation and conduction band profile in the direction of growth related to the device analyzed.

Since the device I am going to describe is unipolar, the valence band is not considered. The description of optical processes in QWs can be tackled using Fermi golden rule (FGR). The transition rate can be expressed as:

$$W_{if} = \frac{2\pi}{\hbar} (| \langle \psi_i | H' | \psi_f \rangle |)^2 \delta(E_f - E_i - \hbar\omega) \quad (2.5)$$

where  $H'$  is the interaction Hamiltonian. The matrix element present in this equation can be split in intra-band and inter-band term; since the QWIP operation exploits the former I am going to focus on this term. Light matter interaction is treated assuming a linearly polarized plane wave  $E = E_0 \vec{e} \cos(q\vec{r})$ , within the dipole approximation. It is possible to rewrite the transition rate as:

$$W_{if} = \frac{2\pi}{\hbar} \frac{e^2 E_0^2}{4m^* \omega^2} (| \langle \phi_i | \vec{e} \cdot \vec{p} | \phi_f \rangle |)^2 \delta(E_f - E_i - \hbar\omega) \quad (2.6)$$

The intra-band or intersubband (ISBT) term consider transitions that occur between levels within the same band. Expanding the ISBT term:

$$\langle f_{nk_{\perp}} | \vec{p} | f_{n'k'_{\perp}} \rangle = \frac{1}{A} \int e^{-ik_{\perp} \vec{r}} \phi_n^*(z) [e_x p_x + e_y p_y + e_z p_z] e^{ik'_{\perp} \vec{r}} \phi_{n'}(z) d^3 r \quad (2.7)$$

It is possible to notice that only the component along the growth direction of the momentum operator yields a contribution at finite frequency. Thus the only matrix elements different from zero for ISBTs are:

$$\langle n | p_z | n' \rangle = \int dz \phi_n^*(z) p_z \phi_{n'}(z) \quad (2.8)$$

These terms constrain the possible transitions and impose two conditions: in order to absorb or emit, the wavefunctions involved should have opposite parities and the electric

field should have a component in the growth direction. These are called Parity and Polarization selection rules for ISBT. After the evaluation of the matrix elements relevant for the ISBT, the absorption coefficient could be obtained through:

$$\alpha_{2D} = \frac{W_{if}\hbar\omega}{AI_{incident}} \quad (2.9)$$

where  $I_{incident}$  is the intensity of the incident radiation and A is the area. It is possible to introduce an oscillator strength to quantify the strength of transition as:

$f_{n,n'} = \frac{2m^*\omega_{n,n'}}{\hbar} \langle z \rangle_{n,n'}^2$ . Inserting it in 2.9 and integrating with respect to  $k_{\perp}^2$ , it is possible to obtain the final formula for the absorption for a single transition:

$$\alpha_{2D} = \log\left(\frac{1 + \exp\left(\frac{E_f - E_n}{k_b T}\right)}{1 + \exp\left(\frac{E_f - E_{n'}}{k_b T}\right)}\right) e^2 k_b T \frac{1}{2\epsilon_0 n_r c \hbar} f_{n,n'} \frac{\gamma / \pi i}{(-\hbar\omega + (E_{n'} - E_n)^2 + (\gamma)^2)} \quad (2.10)$$

The delta function describing energy conservation present inside the FGR has been substituted with a Lorentzian function with Half Width Half Maximum (HWHM)  $\gamma$  to take into account line broadening and finite lifetime of electronic states. The Fermi level is defined through the 2D density of electrons inside the well as :

$$E_f = n_{2D} \frac{\pi \hbar^2}{m^*} \quad (2.11)$$

This is an approximation valid only at low temperature. The absorption coefficient has been computed just for a single transition, since the QWIP device I am going to describe is designed to have only 2 bound states inside the wells, so that photoexcitation is possible through a bound-to-bound transition.

## 2.2 Theoretical description of a QWIP

QWIPs are made of a periodic structure composed of quantum wells. The different wells are separated by a thick barrier to avoid tunnel coupling among the various periods. Two recurrent design strategies are always employed in optimized QWIP detectors regarding the quantum well band structure: a quasi-resonant positioning of the excited state with respect to the barrier to enhance the efficiency of the emission process and a strong doping in the well material to guarantee a population of electrons in the ground state of the wells. The structure is submitted to a voltage, which results in a bending of the band structure, as depicted in 2.3.

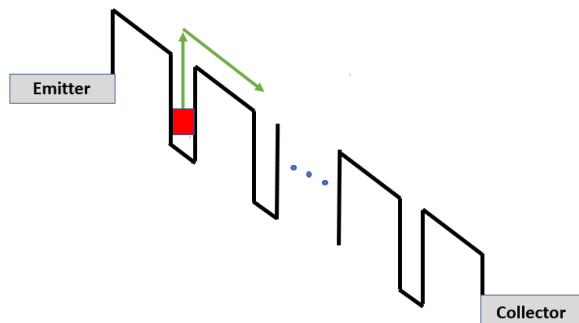


**Figure 2.3:** QWIP device structure.

The device is made of an injecting contact, that serves as first source of electrons to be injected in the wells, and a collector that allows gathering carriers at the end of the device. An important quantity that is crucial to understand the device operation is the dark current density,  $J_{Dark}$ . It is defined as the current that is naturally present inside the device even when no light is shining on it. It is mainly induced by thermal excitation phenomena. Since the device is considered at equilibrium without light shining on it, the carrier density inside the well should be kept constant. This implies an injection of carriers from the contacts that balances the thermoionic emission from the wells, to avoid complete depletion. A sketch depicting the phenomenon can be found in figure 2.4

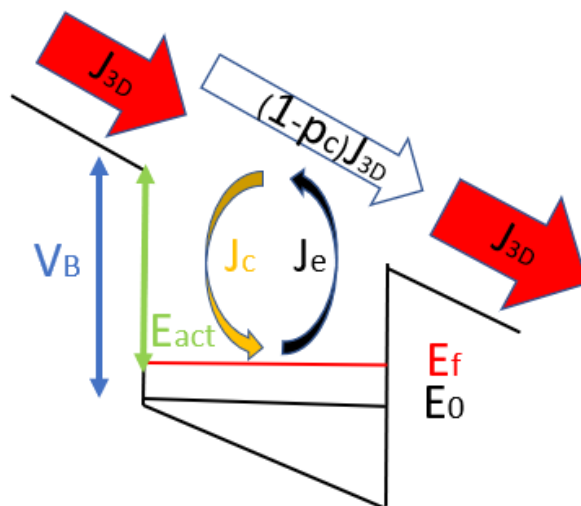


**Figure 2.4:** Schematic of processes in dark condition.

In figure 2.4, it is possible to notice that other two currents should be considered to analyze the device,  $j_e$  and  $j_c$ . They describe the capture and emission of carriers present in the quantum wells. At equilibrium the following relation holds:

$$j_e = j_c \quad (2.12)$$

They describe the two mechanisms that cause the formation of a 3D current above the wells in the device, through the capture or emission probability  $p_c$  and  $p_e = 1 - p_c$ . In order to compute  $J_{Dark}$  there are two models that will be briefly discussed.

### 2.2.1 3D Model

This model describes directly the macroscopic current  $J_{Dark}$ , which is computed as:

$$J_{Dark} = eN_{3D}v_{drift}(E_{field}); \quad (2.13)$$

with  $v_{drift}$  the drift velocity of electrons.  $N_{3D}$  is the most important quantity of the model. It represents the electronic density of carriers thermally excited above the well. Its expression is:

$$N_{3D} = 2\left(\frac{m_b^*k_bT}{2\pi\hbar^2}\right)^{\frac{3}{2}}exp\left(\frac{-E_{act}}{k_bT}\right); \quad (2.14)$$

In equation 2.14 the effective mass considered is the one of the barrier material,  $E_{act}$  is defined as the energy needed to excite carriers out of the wells, it is the difference between the barrier height and the Fermi level as indicated in figure 2.4.

### 2.2.2 Emission capture model

This model computes  $J_{dark}$  starting from  $j_e$ , through the relation  $J_{Dark} = \frac{j_e}{p_c}$ . It considers electrons as emitted out of the well mainly by scattering assisted processes. Moreover, it takes in account the probability of transmission of electrons out of the quantum well,  $D(E, \xi)$ , as function of the energy and the electric field.

The emission current is computed in the following way:

$$j_e = e \int_{E_0}^{\infty} \frac{D(E, \xi)}{\tau_{scattering}} \frac{m^*}{\pi\hbar^2} \left(1 + exp\left(\frac{E - E_f}{k_bT}\right)\right)^{-1} dE \quad (2.15)$$

where  $\tau_{scatt}$  is the scattering time needed to extract electrons out of the well and  $E_0$  is the ground state of the well. The main approximation of the model is the dependence of  $\tau_{scattering}$  on the energy. It is approximated with the lifetime of the carriers,  $\tau_{lifetime}$ , that is the time constant related to the capture process. Once  $j_e$  is found through equation 2.15, it is possible to find  $J_{Dark}$  through the definition of  $p_c$ :

$$p_c = \frac{\tau_{transit}}{(\tau_{transit} + \tau_{lifetime})} \quad (2.16)$$

A new time constant is introduced to define the capture probability,  $\tau_{transit}$ . It is related to the time spent by carriers above the wells and it is directly proportional to the well length and the drift velocity of carriers inside the device. A schematic resuming the time constants inside the device is depicted in figure 2.5

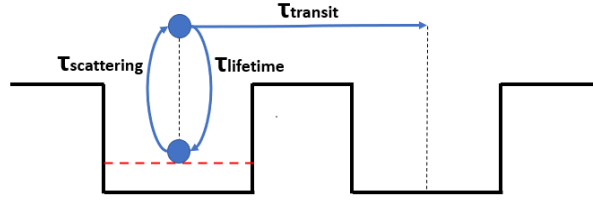


**Figure 2.5:** Time constants in dark condition.

The final expression of the dark current comes out to be:

$$J_{Dark} = ev_{drift} \frac{m_b^*}{\pi \hbar^2 L_p} k_b T \exp\left(\frac{-E_{act'}}{k_b T}\right) \quad (2.17)$$

$L_p$  is the length of one period, it is defined as sum of the length of the barrier and well structure. Equation 2.17 resembles the one in 2.13 with the main difference that the activation energy,  $E_{act'}$ , is computed considering a barrier lowering mechanism due to the application of an external field on the structure.

### 2.2.3 Photocurrent

In the previous section the dark operation of QWIPs has been analyzed. This section describes their operation under illumination. The device is conceived to detect light at specific wavelength defined by the well and by the material system. When an EM radiation is impinging on the detector, another current is generated, the **Photocurrent**. This quantity has to be maximized in order to obtain a good detection of light, since it will be summed to the already described dark current.

The light shining on the device results in a photoemission of carriers outside the well, it can be seen in figure 2.6. It brings an extra injection, trapping and emission inside the structure. Photocarriers extraction mechanisms give rise to a reduction of the resistance in the device that results in an increase of current above the wells.

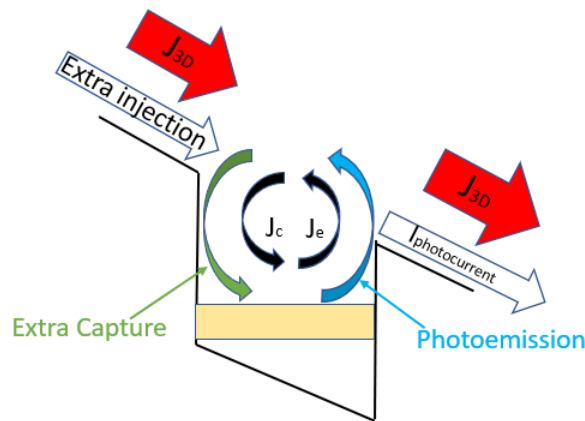


**Figure 2.6:** Schematic of processes under illumination.

The theoretical model that describes the QWIP operation is based on the rate equation related to the photoexcited electrons :

$$\frac{dn_{ex}}{dt} = \Phi\eta - \frac{n_{ex}}{\tau_{escape}} - \frac{n_{ex}}{\tau_{relax}} \quad (2.18)$$

This rate equation takes into account two other lifetimes,  $\tau_{escape}$  and  $\tau_{relax}$ . The former is related to the escape time of carriers from the well, the latter to the intersubband relaxation of carriers between levels. A sketch of the processes is presented in figure 2.7. The first term in equation 2.18 is related to the absorption of the overall structure,  $\eta$ , and  $\Phi$  is the incident flux on the device.

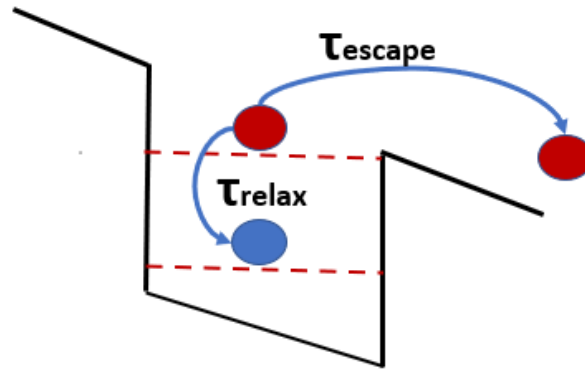


**Figure 2.7:** QW characteristic time constants under illumination.

The value of  $n_{ext}$  is obtained by solving 2.18 at steady state. Then the current generated from one well is calculated and finally the total observed photocurrent is:

$$I_{photo} = e\Phi\eta g_{photo} \quad (2.19)$$

The quantity  $g_{photo}$ , called photoconductive gain, is defined as  $\frac{p_e}{Np_c}$ , with N representing the number of wells inside the structure. It has been found to be proportional to the emission probability  $p_e = \frac{\tau_{relax}}{(\tau_{relax} + \tau_{escape})}$ . Important considerations about the photocurrent are related to its dependence on the number of periods inside the device. It may seem that the more are the periods the more would be the current generated, but inspecting better the equation it is possible to notice that  $\eta$  depends linearly on the wells number,  $\eta = N\alpha_{2D}$ , while  $g_{photo}$  is inversely proportional to it.

This brings to the conclusion that the photocurrent is not dependent on the number of periods.

## 2.2.4 Responsivity

The responsivity is a parameter that measures the detector performance. It is defined as:

$$R = \frac{I_{photo}}{\hbar\omega\Phi} = \frac{\eta g_{photo} e}{\hbar\omega} [A/W] \quad (2.20)$$

where  $\Phi$  is the number of photons per unit time and  $\hbar\omega$  the photon energy. Its magnitude is controlled by both the absorption of the structure  $\eta$  and the photoconductive gain  $g_{photo}$ . A high absorption is not the only controlling parameter since carriers should be able to efficiently escape the wells in order to give rise to a large photocurrent. In order to optimize  $R$ , the excited state of the wells should be quasi-resonant with the barrier edge. This optimization is related to the lifetime of excited carriers. The relation to be satisfied is  $\tau_{escape} < 1ps$ , to obtain  $p_e \approx 1$ . As discussed for the photocurrent,  $R$  is independent on the number of periods inside the structure. The main parameter that influences the responsivity of the detector is the drift velocity of carriers above the wells. This causes  $R$  to be temperature dependent. Moreover, also a voltage dependence is present. The typical behaviour of  $R$  is an increase at lower voltage with temperature until it reaches a turning point where it starts to decrease, while at higher voltages  $R$  tends to decrease with increasing temperature.

## Chapter 3

# Experimental Analysis

### 3.1 Device details

The device is a QWIP that works at  $9 \mu m$ , the substrate chosen is  $InP : Fe$ . The substrate has been doped with Fe to reach a high transmission in the wavelength range of interest. The overall thickness of the substrate is  $300 \mu m$ . The standard material system used for QWIP is  $GaInAs-AlInAs$  lattice matched to  $InP$ , the conduction band offset is set to  $520 meV$ . The material system employed in my device is composed of  $36.7 nm$  barrier made of a quaternary semiconductor,  $(Ga_{0.47}In_{0.53}As)_{0.5} - (Al_{0.48}In_{0.52}As)_{0.5}$  and  $8 nm Ga_{0.47}In_{0.53}As$  well. The quaternary semiconductor has been employed since it possible to tune the barrier height based on the composition of the two ternary material that compose it. The variation of the band offset as function of the composition can be found in figure 3.1. It has been designed with 50% composition, a  $260 meV$  barrier height is expected.

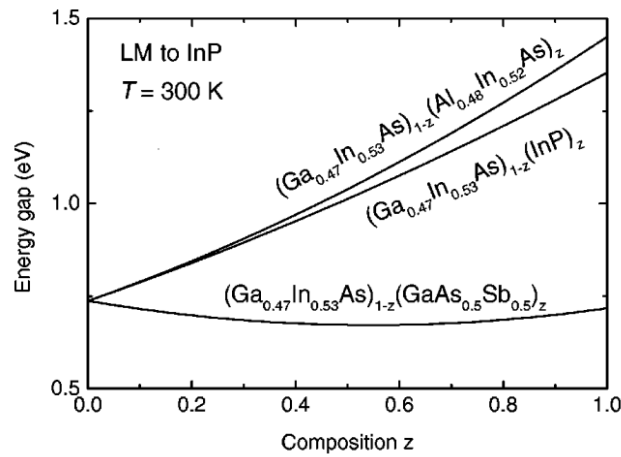


**Figure 3.1:** Variation of energy gap for different quaternary semiconductor compounds as function of composition [4] .

The device is composed of a periodic structure of quantum wells with 13 periods. The wells have been doped, the doping is  $5 * 10^{17} \text{cm}^{-3}$ . Two bound state are theoretically expected inside each well, the transition exploited to detect light is designed to be  $139 \text{meV}$ , it corresponds to  $8.92 \mu\text{m}$ . A simulation has been performed in order to obtain the wells band structure. The method employed to compute it is a shooting method, that takes in account the non parabolicity of the conduction band, as described in [5]. The results of the simulation are displayed in 3.2.

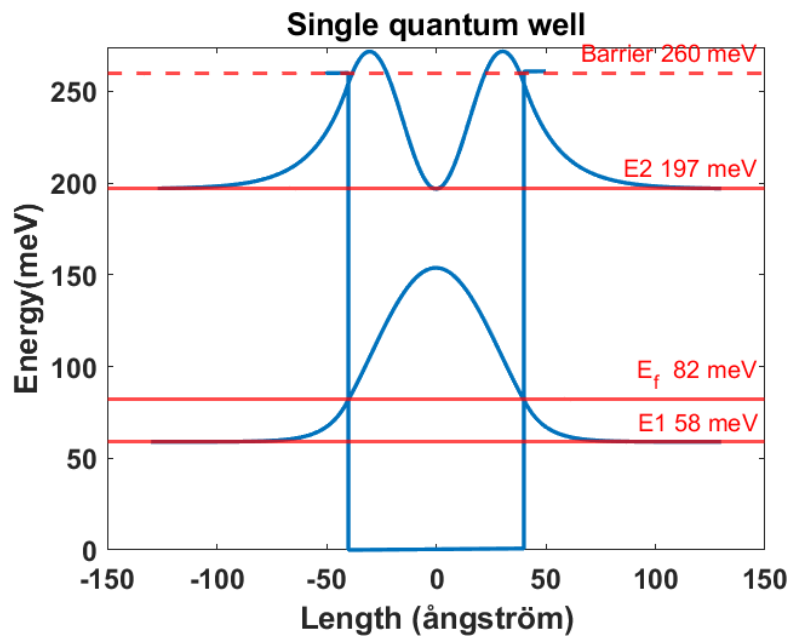


**Figure 3.2:** Simulated quantum well structure of the QWIP device.

### 3.1.1 Absorption profile

The absorption spectrum of the device has been simulated through the formula 2.10. The theoretical absorbance formula has been simplified from the one shown in section 2, taking the limit for  $T=0$ . This allows finding an upper bound for the absorbance of the device, since  $\alpha_{2D}$  decreases with temperature. The implemented formula is :

$$\alpha_{2D} = \frac{n_{2D}e^2\hbar f_{12}}{2\epsilon_0cn_r m^*} \frac{\gamma}{(E_2 - E_1 - \hbar\omega)^2 + \gamma^2} \quad (3.1)$$

The result is shown in figure 3.3. Usually  $\alpha_{2D}$  is expressed in percentage of absorption. The final value at its peak wavelength is found to be 0.97% per well. This value should be multiplied by the number of periods inside the structure to obtain the total absorbance of the device,  $\eta = 12\%$ .

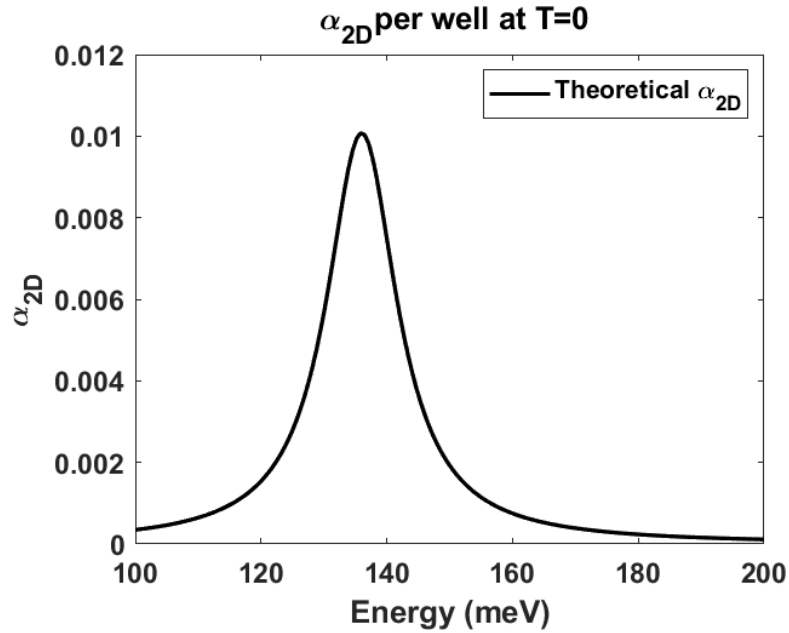


**Figure 3.3:** QWIP theoretical absorbance per well.

The absorption spectrum is measured through a multi-pass experiment. It consists of measuring the transmission of the sample shining light on it and detecting the transmitted radiation with a commercial detector. The geometry chosen for the experiment, performed by Livia Del Balzo, is depicted in figure 3.4.

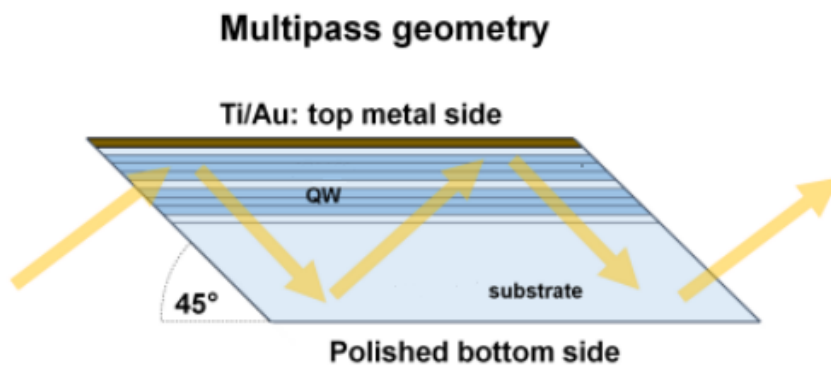


**Figure 3.4:** Absorption experiment geometry [1].

The spectrum measured at room temperature shows a dip of transmission at  $9.48\mu m$ . This corresponds to the peak of absorption of the device, it depends on the temperature of the experiment. The absorption wavelength shifts toward higher  $\lambda$  value at higher temperature. The measured transmission spectrum is shown in figure 3.5.

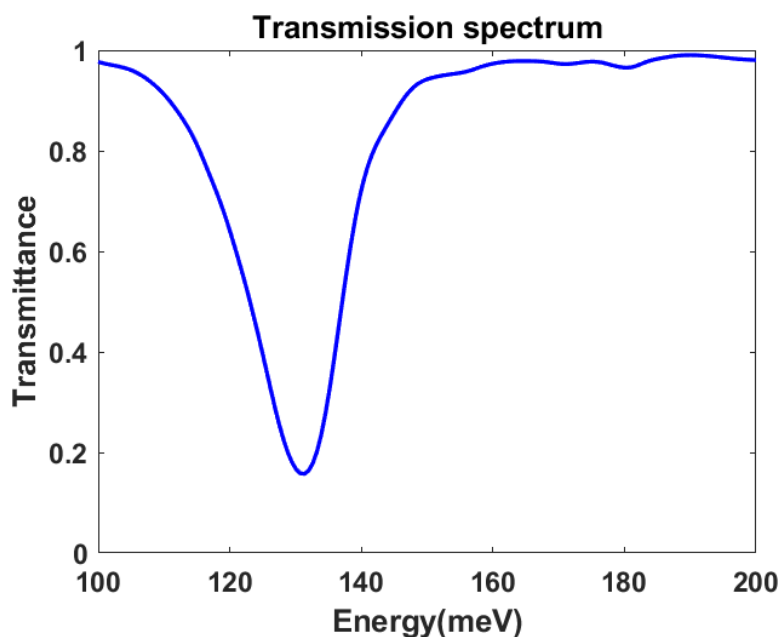


**Figure 3.5:** Transmission profile of the sample.

Once the transmittance is known, it is possible to retrieve the value of  $\alpha_{2D}$  since they are strictly related. Moreover considering the number of times the light and the active layer have interacted, it is possible to find the experimental value of  $\alpha_{2D}$  from:

$$\frac{A \cos(\theta)}{C M_{interaction} \sin(\theta)^2} = N_{well} \alpha_{2D} \quad (3.2)$$

where  $A$  is the absorbance,  $A = -\ln(\text{Transmittance})$ ,  $M_{interaction}$  refers to twice the number of reflections inside the experimental geometry shown in 3.4,  $N_{well}$  is the number of periods,  $C$  is a coupling constant dependent on the boundary conditions. The term  $\frac{\sin(\theta)^2}{\cos(\theta)}$  takes into account the effective interaction of light with the sample considering the angle of incidence and the effective length of interaction.

In order to compare experimental and theoretical absorption spectra of the device, a new simulation with improved parameters has been performed, taking in consideration the data obtained in section 3.4 and 3.3. Two elements were targeted for the new simulation: the activation energy and the transition energy  $E_{12}$ . The former has been experimentally evaluated to be  $140\text{meV}$  at low bias, while the latter  $136\text{meV}$ , as it will be discussed later. The tuning parameters for the simulation are the quaternary material composition, and the quantum well thickness. The quaternary material composition has been found to be  $(\text{Ga}_{0.47}\text{In}_{0.53}\text{As})_{0.57} - (\text{Al}_{0.48}\text{In}_{0.52}\text{As})_{0.43}$  and the well's dimension  $7.7\text{ nm}$ . This tuning allows matching the simulation with my experimental results. The simulation outcome is shown in figure 3.6. The new transition energy allow to define the detection wavelength of the device,  $9.12\mu\text{m}$ . Moreover the second level is found to be  $26\text{ meV}$  below the barrier, this shows that the quasi-resonant condition with the barrier has not been achieved perfectly.

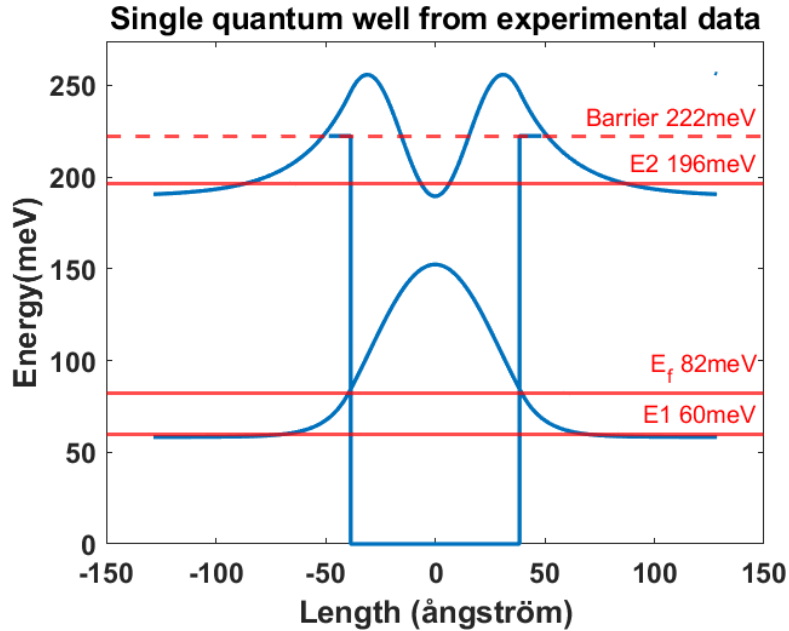


**Figure 3.6:** Simulated QW bound states after parameters adjustment.

Once the experimental band structure has been obtained, it was possible to compute the theoretical absorption spectrum, through equation 3.1, and compare it with the experimental result obtained through equation 3.2. The parameters used to evaluate the

absorption can be found in table 3.1.

$\gamma$	13.64 meV
$f_{12}$	0.8
$E_{21}$	136.4 meV
$n_{2D}$	$4 * 10^{11} \text{ cm}^{-2}$

**Table 3.1:** Theoretical parameter inserted in equation 3.1.

. The comparison is plotted in figure 3.7.

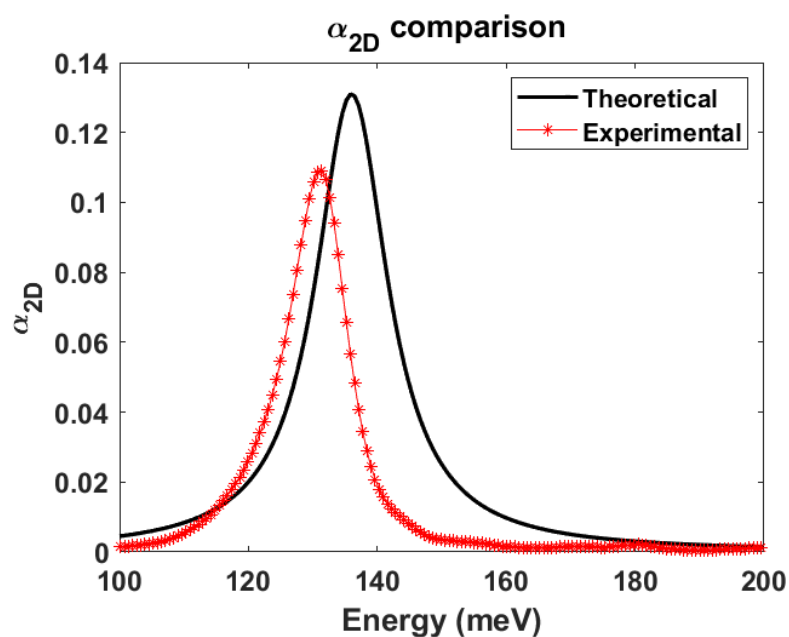
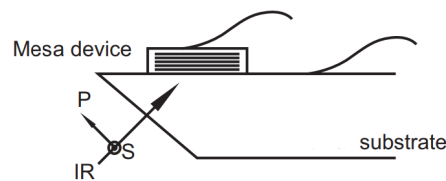


**Figure 3.7:** Theoretical vs experimental  $\alpha_{2D}$ .

It is noticeable that the peak of the simulated  $\alpha_{2D}$  is higher than the experimental one. Moreover, the two peaks are displaced with respect to each other, this effect is mainly due to a temperature-dependent red shift of the absorption at higher temperatures.

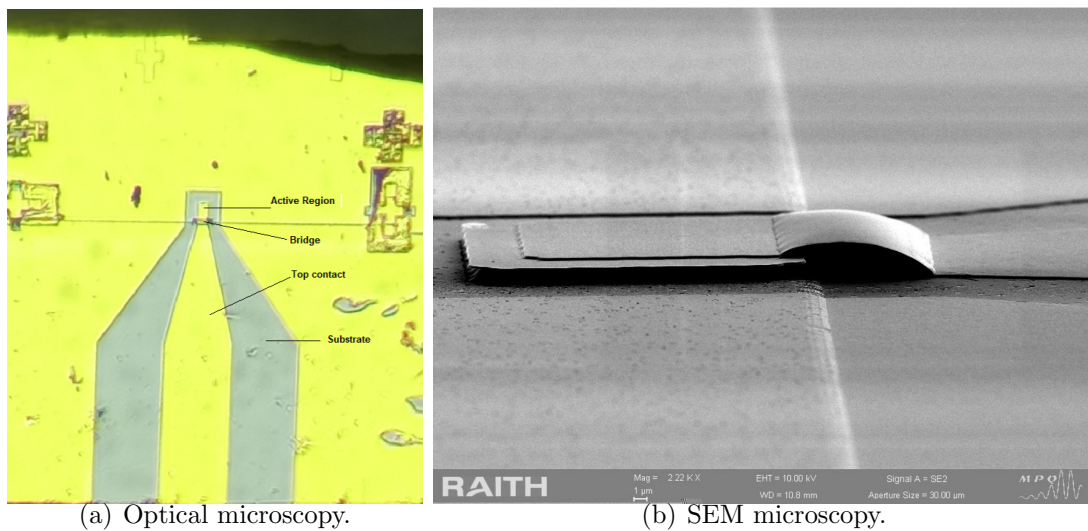
## 3.2 Mesa geometry

Figure 3.8 sketches the geometry of the device used for the measurements, the device presents a  $45^\circ$  facets. This choice has been employed to be compliant with the Polarization selection rules described for ISBT. This geometry allows light polarized parallel to the facet, p-polarized light, to have a component in the growth direction when it interacts with the active region.



**Figure 3.8:** Device geometry [3] .

Two Au contacts have been deposited, both of them on top of a  $n^+$  doped region, below and above the active region. Moreover an air bridge has been employed, it connects the mesa with a coplanar waveguide for high frequency operation. A gold wire bonding to the contacts has been performed to allow the electrical characterization of the device. The device and a zoom on the bridge are shown in figure 3.9.



**Figure 3.9:** On the left an optical microscopy image of the device. On the right a Scanning Electron Microscopy image of the bridge.

### 3.3 I/V characteristic

The measurements performed in this section are related to the electrical characterization of the QWIP in dark conditions and under illumination by a laser source at  $9.12\mu m$ .

#### 3.3.1 Dark current

The dark current measurements have been performed with the QWIP inside a cryostat, to analyze the device's electrical behaviour as function of the temperature. A cryoshield has been inserted inside the cryostat in order to avoid background radiation from objects surrounding the QWIP itself at higher temperature than the device. A pump was used to reach vacuum inside the chamber and liquid nitrogen has been employed as cryogenic fluid to reach the minimum temperature of 78K. In order to obtain stable and clear results, the nitrogen was poured inside the chamber with a transfer line connected to a nitrogen tank, to control the  $N_2$  flux. The temperature was kept constant with time through a temperature controller, to select the temperature for the experiment. The I/V curves have been obtained through a Keithley multimeter controlled by a python script to swap the voltage from  $-2V$  to  $2V$ . The QWIP response as a function of voltage and temperature permits to compute the activation energies present in both equation 2.17 and 2.13. This quantities have been evaluated after taking the I/V at different temperatures, fixing the voltage and interpolating the points as function of temperature. The I/V curves as function of the temperature are plotted in figure 3.10. It can be

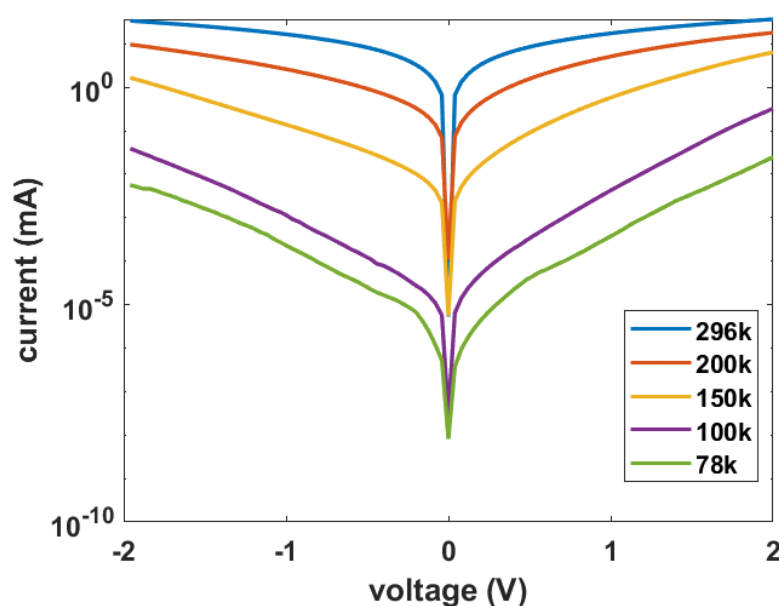
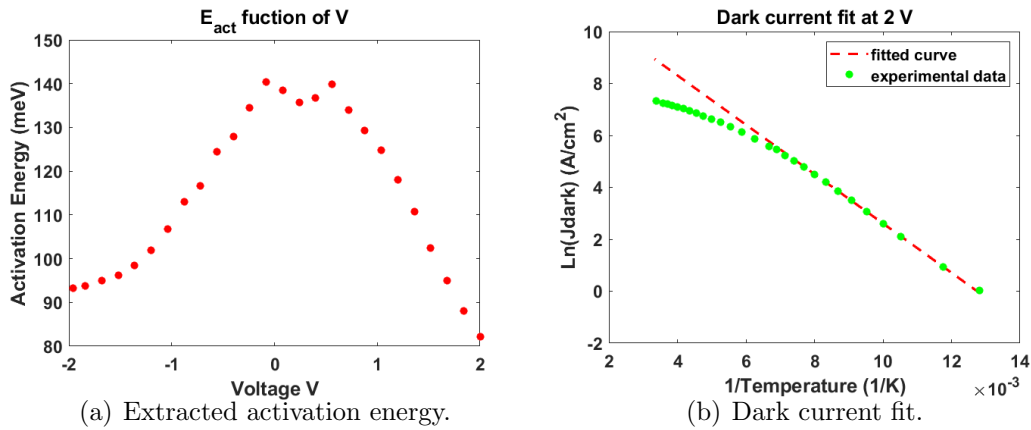


Figure 3.10: Dark current as function of voltage at different temperatures

noticed a strong dependence of the magnitude of  $J_{Dark}$  on temperature as expected. As  $T$  increases, the current inside the device increases exponentially as described in Chapter 2. The curves were measured from 78K to 293K. The points considered for the extraction of the activation energy are in the range [78K,130K]. Points outside this range have been excluded since strong temperature activated phenomena starts to be dominant at higher temperatures. This affects the shape of the curves and it could drive the device out of its ideal behaviour. An example of the fitting result at 2V is presented in figure 3.11(b) The extracted values of the activation energy are depicted in figure 3.11(a),  $E_{act}$  is decreasing with increasing voltage. The voltage tilts the band structure of the wells, allowing thermally excited carriers to be transmitted more easily across the barrier, so favouring the extraction of electrons. It is noticeable a slight asymmetry in the trend of  $E_{act}$  and in the I/V curves probably caused by a difference in the contacts.



**Figure 3.11:** The left figure shows the extracted values of the  $E_{act}$ .The right image shows the fitting curve obtained at 2V.

The value at low voltage,  $140\text{meV}$ , has been taken as activation energy to perform a fit of the I/V curve at 78K with the two models presented in section 2. The value of the current at 78K is plotted with the Emission-Capture and 3D model in figure 3.12. The data needed to evaluate the formulas of  $J_{Dark}$  have been taken from [6] and [7] through an interpolation between the two ternary materials present in the quaternary barrier. They are listed in table 3.2.

$m_b^*$	$0.05m_0$
$\mu$	$3000 \frac{cm^2}{V \cdot s}$
$L_p$	$44.7 nm$
$E_{act}$	$140 meV$

**Table 3.2:** Parameters of emission capture and 3D model inserted in the reference equation 2.17 and 2.13.

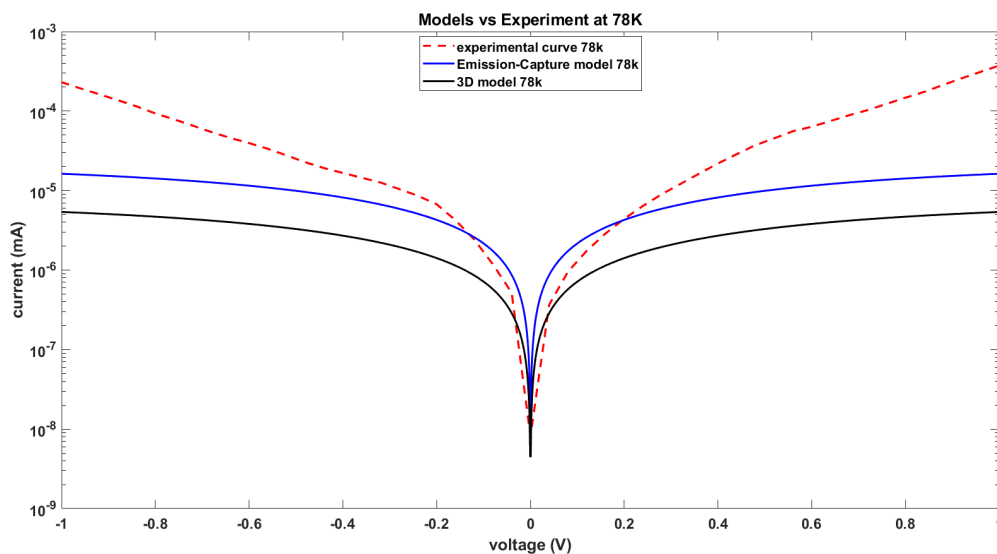


**Figure 3.12:** I/V comparison between experimental data (red), Emission capture model (blue) and 3D model (black) at 78K.

The two models can reliably reproduce the device I/V characteristic at low voltage values. It is noticeable that at higher voltages both models diverge with respect to the behaviour of the QWIP.

### 3.3.2 Photocurrent

The successive evaluation of the I/V curves under illumination has been performed with a Mircat external cavity quantum cascade laser shining on the sample, at the peak of absorption of the device,  $9.12\mu m$ . The sample was inserted in the cryostat without shield, the laser beam was directed toward the sample through a periscope, that allows tilting the polarization of the Mircat laser in order to comply with the Polarization selection rules. With the help of a gold mirror, the beam was deviated toward a 2" F1 Germanium lens. The device has been aligned through a Lock-in technique, in order to position the QWIP in the focal point of the lens. Moreover the positioning of the cryostat has been set by a 3D axis. A schematic of the set up is shown in figure 3.13.

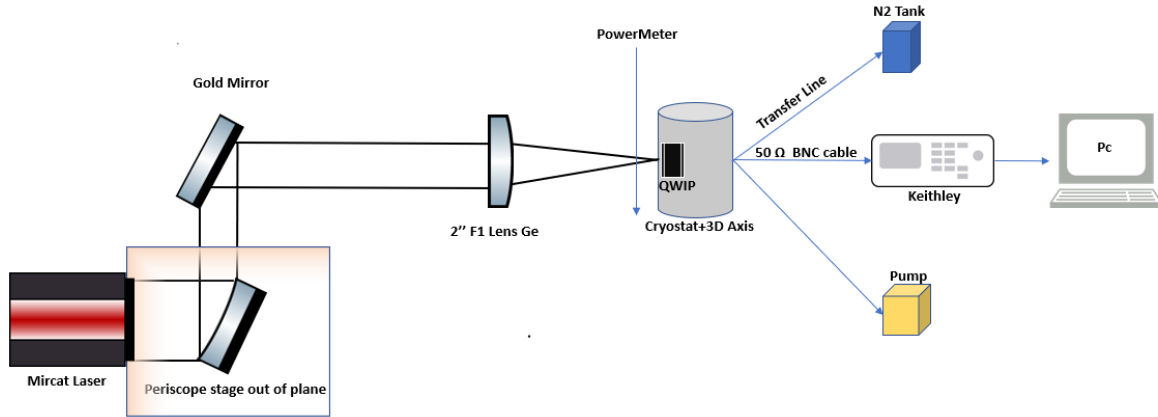


**Figure 3.13:** Experimental set-up.

The effect of the laser shining on the sample is to generate a photocurrent,  $J_{photo}$ , that adds to the existing  $J_{Dark}$ . The results are displayed in figure 3.14. The procedure to obtain it is a subtraction of the currents obtained with the laser and the bare dark current measurements.

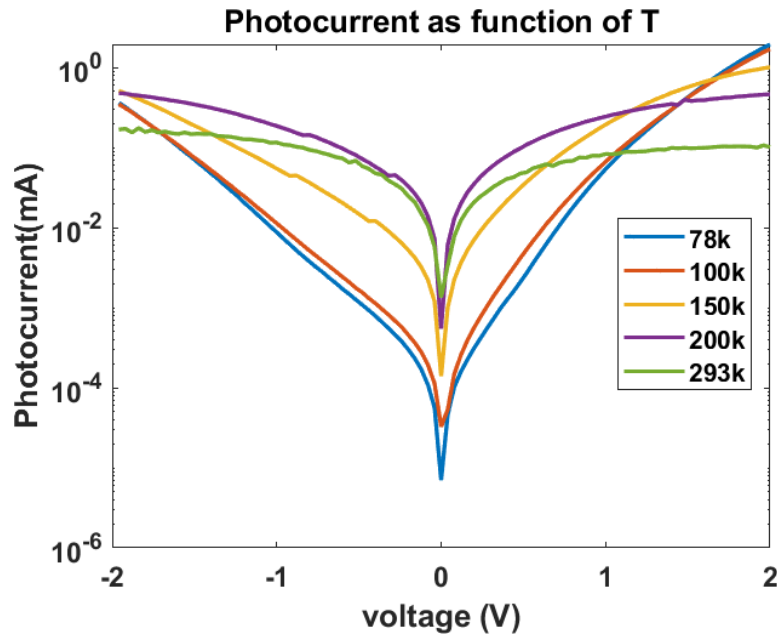


**Figure 3.14:** Photocurrent as function of voltage for different temperatures.

There are three main mechanisms that define the behaviour of the  $J_{photo}$  as function of temperature: the first is related to the 2D population of the wells, that decreases with temperature. The second is related to the exponential increase of the dark current that is "washing away" the effect of photogeneration inside our device. The third is strictly related to the electronic transport inside the device that depends on temperature. The

trend noticeable in 3.14 is an increase of  $J_{photo}$  until 200K at small voltage values, while for higher voltage  $J_{photo}$  is higher at lower temperature. The complete I/V curves under illumination are compared with the Dark current ones in figure 3.15.

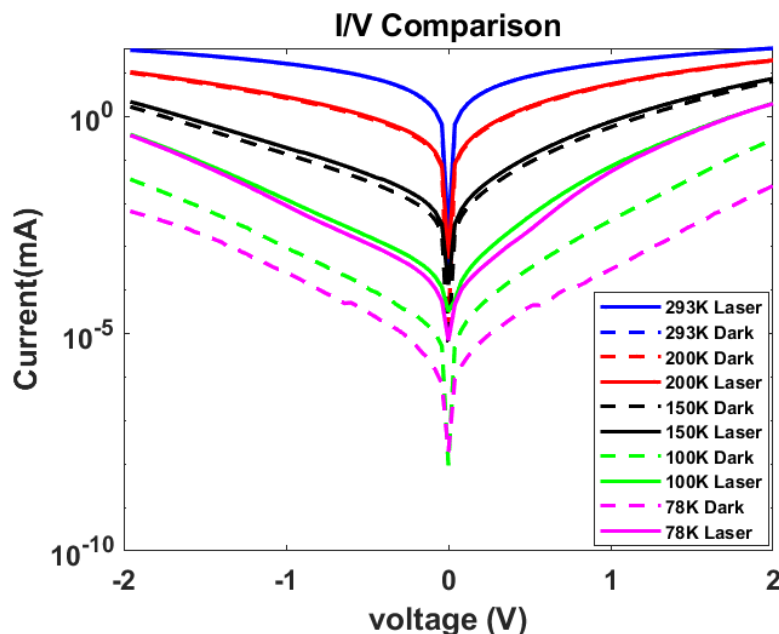


**Figure 3.15:** Comparison between I/V curves under laser illumination and in dark condition.

### 3.4 Spectral characterization of the QWIP.

The spectrum of the device has been measured through Fourier Transform Infrared (FTIR) spectroscopy. This technique allows characterizing the spectrum of a light source or, if the source is known, it is possible to characterize the absorption spectrum of a sample. The working principle is that of a Michelson interferometer that modulates the light source through its movable mirror. The light impinging on the device creates an interferogram on the detector. Theoretically it can be shown that this quantity is related to the Fourier transform of the source spectrum. Since the QWIP should act as a detector, performing the Fourier transform of the interferogram allows finding the photocurrent spectrum of my sample. The spectra were measured as function of temperature and voltage.

#### 3.4.1 Voltage dependence

The experiments have been performed at a fixed temperature, 78K, swapping the voltage value from 0.1V to 2V, with the QWIP inside the cryostat in order to reach the target temperature. The light that impinges on the device comes from a black body source placed inside the FTIR and focused on the sample through an F1 Ge lens. A beam chopper has

been employed to modulate the light beam during the Lock-in alignment procedure. The spectra at lower voltage show two peaks, one related to the designed ISBT transition, the other is still under investigation. The voltage value has been increased until the transition at  $136.4 \text{ meV}$  became dominant. The spectrum at  $2\text{V}$  matches the desired behaviour, the figure is displayed in 3.16(a). It is possible to notice the high energy shoulder that corresponds to the second peak cited above.

Once the voltage has been set, the polarization dependence of the QWIP was analyzed. The FTIR light incident on the device has been polarized through a grid polarizer. The device has been firstly shined with the p-polarized light(TM), then the experiment was performed with s-polarized light(TE), as shown in reference figure 3.8. The results of the experiments are shown in figure 3.16(b). It is noticeable that in the TE configuration the signal is mostly noise. In the p-polarized case the signal shows the characteristic peak of the QWIP, at  $2\text{V}$ ,  $136.4\text{meV}$ .

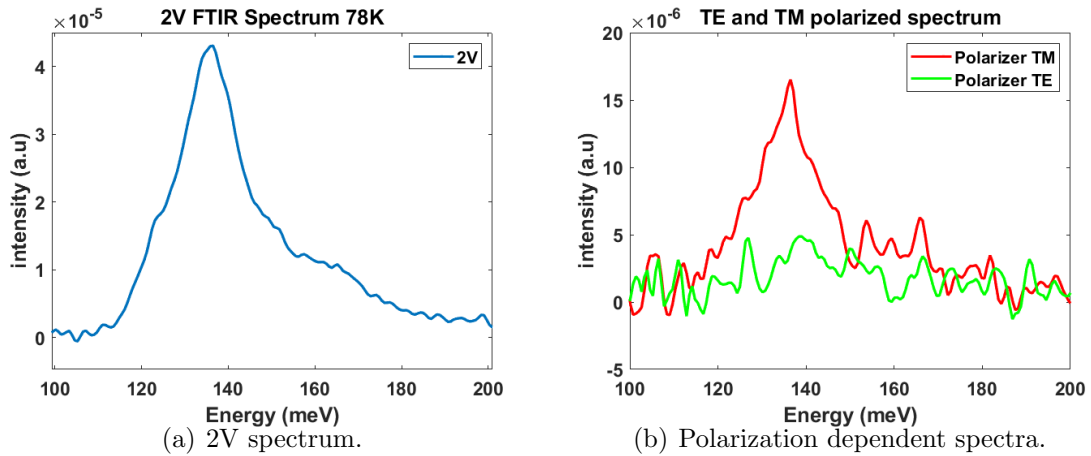


**Figure 3.16:** The left image shows the spectrum obtained with the FTIR experiment at  $2\text{V}$ . The right image compare the two spectra with TE and TM polarized light.

The results obtained have been compared with the absorption spectrum presented in 3.1.1, for consistency. The comparison is shown in figure 3.17. The red shift in the peak energy is a temperature related effect as explained in 3.1.1. The FTIR spectrum shows a larger broadening, since the experiment is dependent not only on the material system absorption but also on the electronic transport inside the device.

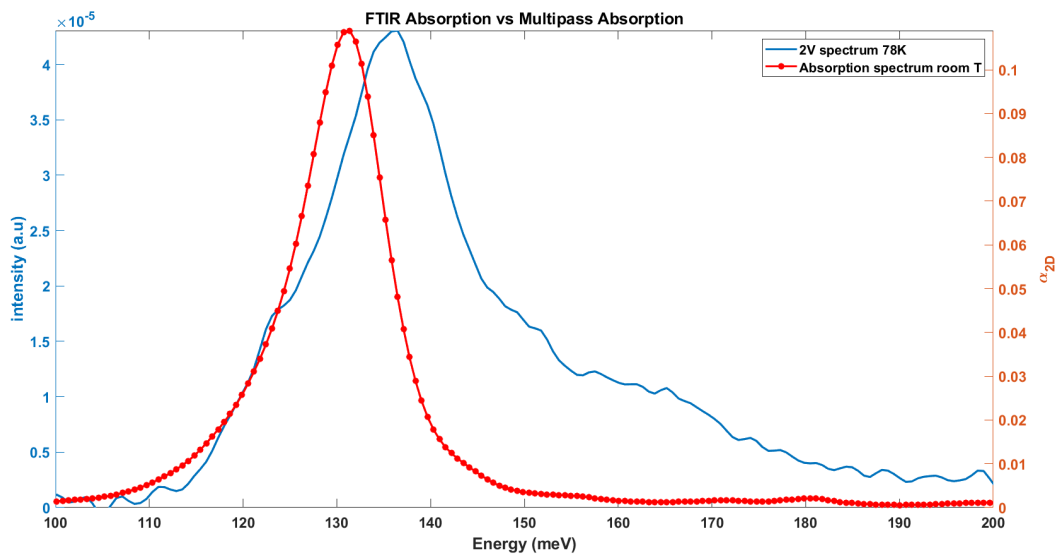


**Figure 3.17:** FTIR and Multi-pass absorption spectra compared.

### 3.4.2 Temperature dependence

The temperature dependence of the spectra taken at 2V have been analyzed through the same set up of section 3.4.1. The results are shown in 3.18. The intensity of the spectral response is decreasing with increasing temperature. This is related to the efficiency of extraction of carriers, the absorption of the structure and the mobility of the carriers inside the device.

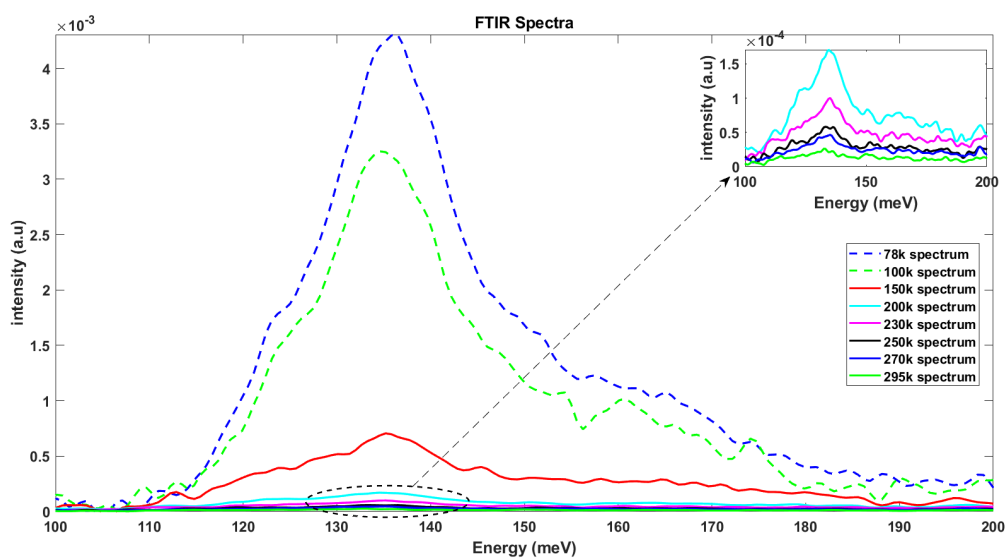
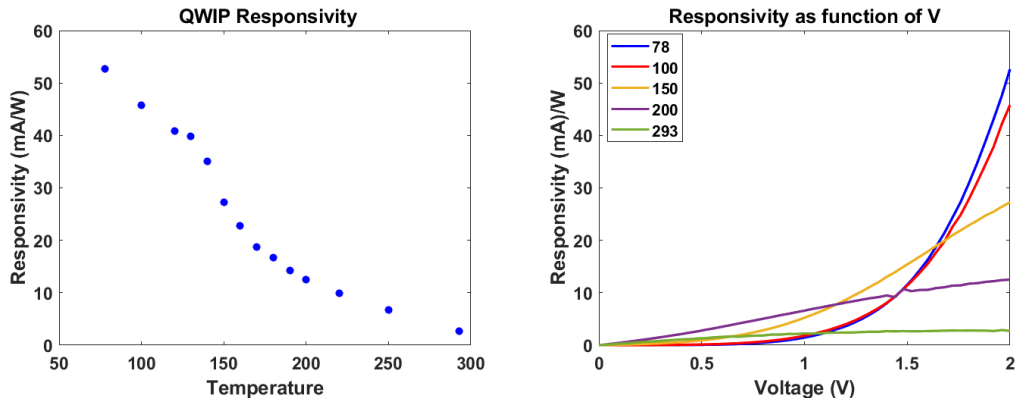


**Figure 3.18:** Spectra as function of T. The inset shows spectra at higher temperature from 200K to 293K.

The peaks loose more than 1 order of magnitude in intensity above 150K. However at higher temperature the ISBT peak is still dominant in its spectral range. As temperature increases is possible to see a tail that is increasing at higher energy.

### 3.5 Responsivity

The responsivity has been evaluated dividing the value of the measured photocurrent by the Mircat laser power incident on the device. The laser power has been measured with a powermeter positioned before the sample. The results obtained match the expected behaviour of  $R$  with temperature.  $g_{photo}$  and  $\eta$  are the two parameters that control the behaviour of  $R$  as temperature is changed. The former is dependent on the time constants of the processes inside the QWIP. The latter is related on how the 2D electron population in the wells is changing with temperature. The results at 2V are plotted in figure 3.19(a). It is noticeable the decrease of the device responsivity with temperature.



(a) Responsivity values at different temperatures. (b) Responsivity curves as function of voltage at different temperatures.

**Figure 3.19:** The left figure show the  $R$  as function of  $T$  at 2V, the right one is showing the trend of  $R$  with voltage at different temperature

The responsivity has been evaluated also at different voltages. The measurement results are shown in figure 3.19(b). It is noticeable that, as expected, the curves as function of the voltage follow the behaviour described for the voltage dependent photocurrent in section 3.3.2.

## Chapter 4

### Conclusions

This internship has revolved around the new material system employed to fabricate the detector, based on a quaternary barrier. It allows to unlock different detection wavelengths that could not be obtained with standard material system on InP substrate. The results presented are however below the expectations in terms of responsivity, for this reason they will be compared to another QWIP device of the same batch. The next step would be to study the same material system inserted in a cavity to enhance the light matter interaction. These devices are already under investigation in the QUAD group with promising future perspectives for the next generation of detectors. The characterization in the lab during the internship has been fundamental to understand how to work with detectors and lasers. It gave me the opportunity to learn how to combine experimental results and theoretical modelling. Moreover it taught me how research project works, that I personally consider the most important aspect for my future working career. In conclusion, I would like to thank the hosting QUAD group for the opportunity given and the skills and advice they conveyed to me.

## Bibliography

- [1] H. C. Liu. Quantum Well Infrared Photodetector Physics and Novel Devices, Chapter 3. *Springer edition*, 2000.
- [2] Daniele Palaferri. Antenna resonators for quantum infrared detectors and fast heterodyne receivers. 2018.
- [3] Roberto Paiella. Intersubband Transitions in Quantum Structures, 1st edition . 2006.
- [4] L. R. Ram-Mohan I. Vurgaftman and J. R. Meyer. Quantum Well Infrared Photodetector Physics and Novel Devices, Chapter 3. *Journal of Applied Physics*, 2000.
- [5] Jérôme Faist Carlo Sirtori, Federico Capasso. Non Parabolicity and sum rule associated with bound-to-bound and bound-to-continuum Intersubband transition in quantum well . *Physical Review Letters*, 1994.
- [6] et al. J. P. Praseuth M. C. Joncour J. M. Gérard. Growth and characterization of AlGaInAs lattice matched to InP grown by molecular beam epitaxy . *Journal of Applied Physics*, 1988.
- [7] Sadao Adachi. III-V Ternary and Quaternary Compounds. *Springer*, 2017.